Performance of automatic exposure control on dose and image quality: comparison between slot-scanning and flat-panel digital radiography systems

Guillaume Boissonnat, Pierre Morichau-Beauchant, Aymeric Reshef, Coralie Villa, Pascal Desaute, Anne-Catherine Simon

Performance of automatic exposure control on organ dose, effective dose, and image quality: a comparison between EOSedge™ and digital radiography

Guillaume Boissonnat,[1] Pierre Morichau-Beauchant,[2] Aymeric Reshef,[2,*)] Coralie Villa,[2] Pascal Désauté,[2] and Anne-Catherine Simon[1]

[1)] *Université Paris-Saclay, CEA, List, F-91120, Palaiseau, France*

[2)] *EOS imaging, 10 rue Mercœur, 75011 Paris, France*

(Dated: 4 July 2022)

Background: EOSedge™[a] (EOS Imaging, Paris, France) is an X-ray imaging system using Automatic Exposure Control (AEC) with tube current modulation, in order to optimize dose deposition in patients.

Purpose: This study aims at characterizing EOSedge organ dose deposition in comparison to a Digital Radiography (DR) system and the previous EOS system (EOS-1st generation), in relation to their respective image quality levels.

Method: Organ doses were measured in an anthropomorphic female adult phantom and a 5 years old pediatric phantom using Optically Stimulated Luminescence dosimeters (OSL), which were carefully calibrated within the studied energy range. Organ doses were recorded on the EOSedge and the Fuji Visionnary DRF (Fujifilm Medical Systems U.S.A., Inc, Lexington, MA). The resulting effective doses were compared to the EOS-1st generation values present in the literature. Image quality assessment was carried out on end-user images. Quantitative image quality metrics were computed for all tested modalities on a quality assurance phantom. Qualitative assessment of EOSedge image quality was based on anthropomorphic phantom acquisitions against the EOS-1st generation system, and on clinical images against the tested DR system.

Results: For a Full-Spine exam, and on the female adult phantom (resp. the pediatric phantom), an effective dose of 92 μSv (resp. 32 μSv) was obtained on EOSedge, and 572 μSv (resp. 179 μSv) on the DR system; these values were compared to effective dose values of 290 μSv (resp. 200 μSv) from the literature on EOS-1st generation, leading to an effective dose reduction factor of 6 with respect to the DR system, and of 3 to 6 with respect to EOS-1st generation. EOSedge provides the best compromise between contrast-to-noise ratio (CNR) and dose, with more consistent CNR values than the other tested modalities, in a range of attenuation from 10 cm to 40 cm of poly(methyl methacrylate) (PMMA). Within this range, EOSedge is also comparable to DR for 10 cm and 20 cm of PMMA, and better than DR for 30 cm and 40 cm of PMMA, both in terms of spatial resolution and low-contrast detection. The anatomical landmarks of interest in the follow-up of spinal deformities can be detected in all tested modalities.

Conclusion: Results showed that EOSedge provides significant dose reduction factors for full spine imaging in both adults and children compared to the other tested modalities, without compromising image quality. We believe that this work could help raise awareness on the capabilities of modern X-ray systems, when equipped with appropriate AEC strategies, to perform ultra low-dose, long-axis images.

Keywords: EOSedge, Flex Dose, X-rays, AEC, Dose, OSL, EOS, DR, Low-dose, Micro-dose, Image quality

I. INTRODUCTION

Patients with spinal deformities are frequently exposed to X-ray exams during the follow-up of their pathologies[1,2]. Exposure to ionizing radiation increases the risk of developing cancer, especially for young populations[3,4]. For instance, young scoliotic female patients may undergo many X-ray exams, leading to an increased risk of developing breast cancer[5]. Moreover, evolutive pathologies such as cerebral palsy or early onset scoliosis also require biplanar X-ray spine exams for both the evaluation and the follow-up of juvenile patients (3 to 9 years old), due to high risk of respiratory impairment[6,7], hence increasing cancer risk and mortality when they are adults[2]. Hence, there is a general tendency of manufacturers to further improve their patient dose reduction strategies. Currently, the main standard of care for follow-ups of spinal deformities is planar radiography, which includes Computed Radiography (CR) or Digital Radiography (DR)[2]. In addition, an increased usage of the EOS biplanar slot-scanning X-ray system (EOS Imaging, Paris, France, referred to as EOS-1st generation system) has been reported for global postural assessments and follow-up of spinal deformities in care, with minimized patient exposure compared to planar radiography[8–14]. In particular, Damet *et al.*[12] and Pedersen *et al.*[13] measured organ dose distribution in the EOS-1st generation system and demonstrated organ dose reduction using low-dose and micro-dose protocols compared to CR and DR. Yet, Pedersen *et al.*[13] still advocated *"continuously work[ing] towards minimizing the total radiation dose to which we expose our patients"*.

*)Author to whom correspondence should be addressed. Electronic mail: areshef@eos-imaging.com

a)EOSedge™ and Flex Dose™ are trademarks or registered trademarks of the company EOS Imaging.

Standard radiography systems and CT scanners tend to have declining exposure, thanks to the development of Automatic Exposure Control (AEC)[15–28].

Standard radiography AEC adjusts exposure time based on a subregion of the exposed patient area. Due to the limited cell dimensions and to the averaging of the dose measurement over the cell size, the advantage of AEC is not fully exploited. In the case of long-axis imaging (Full-Spine, Full-Body, or Lower-Limb imaging), some DR systems enable a stitching option, where the system acquires images at multiple altitudes in a stop-and-shoot manner, which are then stitched together into a single image. In such cases, dose is optimized for each shot.

In contrast, CT AEC is based on a previously acquired, very low dose scout view[29], from which the tube current modulation is calculated based on a predefined detector signal target, and used during the actual CT scan. AEC may enable longitudinal tube current modulation, angular tube current modulation, or both[29].

AEC is now available on most of the CT scanners and standard radiography systems. Literature reports dose reductions ranging from 35 % to 60 %[15] in CT scanners with an active AEC.

In 2019, EOS Imaging introduced the EOSedge system, embedding an AEC, called Flex Dose™a[8,30]. The system aims at reducing patient dose while keeping a constant detector signal over the entire body.

To our knowledge, EOSedge is the only slot-scanning system capable of full-body acquisition with a continuous AEC along the scan. Flex Dose could further reduce the risk from radiation-induced cancer; however, dose performance on this imaging system has not been evaluated yet. This study provides a quantitative investigation of organ dose distribution (including the influence of patient positioning) in EOSedge, and compares it to results obtained on a DR system, and to previously reported values from Damet *et al.*[12] and Pedersen *et al.*[13] on an EOS-1st generation system. In addition, an image quality assessment was carried out in order to study the impact of dose reduction strategies on the clinical use of end-user images. Image quality was quantitatively assessed on a quality assurance phantom, and qualitatively assessed on an anthropomorphic phantom against EOS-1st generation, and on clinical images against DR.

II. MATERIALS & METHODS

A. Flex Dose

In long-axis DR images, stop-and-shoot acquisitions followed by image stitching may be performed with decreasing vertical spreads of the X-ray beam[31], resulting in smaller active detector heights (and more shots), in order to improve scatter rejection and to reduce geometric deformations due to the X-ray cone beam shape.

As the active detector height gets smaller, the X-ray cone beam becomes a fan beam, and the stop-and-shoot strategy is replaced by a continuous vertical motion[1,11]. Such systems are referred to as slot-scanning systems.

When equipped with an AEC, a slot-scanning system should optimize both the tube current profile along the vertical scan, as well as the scan speed. To this end, and similar to what is performed in CT, EOSedge acquires a preliminary low dose scout view; it is used to automatically extract a profile-of-interest along the axial skeleton, on which an equivalent patient thickness is estimated.

The maximum value of this thickness profile and the selected protocol are used to obtain the optimal spectrum according to a reference anatomical parameter table, which defines additional spectral flat filtration and kVp values. Finally, the constant scan speed and the view-dependent tube current profiles are determined in order to optimize the X-ray flux and achieve a detector target signal along the profile-of-interest. When simultaneous biplanar acquisitions are performed, tube current modulation is adapted to each view separately.

B. Dose measurements

1. OSL technology

As described by Bøtter-Jensen *et al.*[32], Optically stimulated luminescence (OSL) is the luminescence emitted from an irradiated insulator or semiconductor during exposure to light. The OSL intensity is a function of the radiation dose absorbed by the sample. Carbon-doped aluminium oxyde ($Al_2O_3:C$) OSL dosimeters are similar to Thermo-Luminescent Dosimeters (TLD) that used to be the standard in dose measurement[12,13]. Yet, unlike OSL where the read-out process is only via light stimulation, TLD requires heating process, thus reducing sensitivity of the dose measurement[32]. Hence, OSL technology was used in this work. However, OSL calibration requires more attention than TLDs in order to get reproducible measures due to the over-response of low-energy X-rays[33].

2. OSL calibration method

OSL dosimeters were read using the reader's high intensity mode (mode dedicated to low doses), performing read-out at least thirty minutes after irradiation to avoid the well documented fading effects[34,35]. Since the successive readout process only decreases signal by approximately 0.8 %[34,35], measurements were averaged over three consecutive readouts to reduce uncertainty. If OSL dosimeters are well suited for low dose measurements, they are known to be very energy dependent in the kV energy range. Therefore, it is necessary to calibrate dosimeters precisely for each measurement beam quality.

a. Beam Quality Calibration Farmer type ionization chambers are used as standard ionization chambers for

absolute dose measurements in radiation therapy. Assuming that such a dosimeter is well calibrated within the desired kVp range, the air-kerma value measured by the ionization chamber $K_{\text{air}}^{\text{IC}}$ is obtained. The OSL signal measure s_{OSL} needs to be corrected by the baseline and the sensitivity at the measured beam quality Q according to Equation (1):

$$D_{\text{air}}^{\text{OSL}}(Q) = f_Q \times s_{\text{OSL}} \tag{1}$$

Once corrected, the calibration ratio f_Q is defined as in Equation (2):

$$f_Q = \frac{K_{\text{air}}^{\text{IC}}}{s_{\text{OSL}}} \tag{2}$$

b. Dose to Medium The dose to medium D_m is derived from the dose to calibration medium (air in our case) using the mass energy absorption coefficient (μ_{en}/ρ) ratio between the medium and air at a given beam quality as expressed in Equation (3):

$$D_m(Q) \approx D_{\text{air}}(Q) \times \left(\frac{\left(\frac{\mu_{\text{en}}}{\rho}\right)_m}{\left(\frac{\mu_{\text{en}}}{\rho}\right)_{\text{air}}} \right)_Q \tag{3}$$

This correction is especially important for bones (as the effective atomic number deviates from air) and for low kVp values[35,36].

In order to obtain the dose in medium at the point of measurement from a detector calibrated in dose in air, one should correct from the difference of the OSL dosimeter sensitivity between the incident beam quality (Q) and the beam quality at the point of measurement (Q') as expressed in Equation (4):

$$D_m(Q') \approx D_m(Q) \times f_{Q,Q'} \tag{4}$$

with

$$f_{Q,Q'} = \frac{\left(\frac{\left(\frac{\mu_{\text{en}}}{\rho}\right)_m}{\left(\frac{\mu_{\text{en}}}{\rho}\right)_{Al_2O_3:C}} \right)_{Q'}}{\left(\frac{\left(\frac{\mu_{\text{en}}}{\rho}\right)_m}{\left(\frac{\mu_{\text{en}}}{\rho}\right)_{Al_2O_3:C}} \right)_{Q}} \tag{5}$$

3. Effective dose

Dose for each organ was computed as the mean value of the dose values measured by the OSLs in the given organ. Effective dose was computed according to the International Commission on Radiological Protection 103 recommendations[37].

Specific organs were excluded from the study, especially organs where dose was not measured (lymphatic nodes for example) or distributed "organs", such as bone surface and skin where the computation was not possible due to the limited points of measure. Thus, the sum of the weight factors for the considered organs reached 0.97.

The details of the weighting factors are available in Tables X and XI from Appendix B.

C. Dose experiments & set-up

1. Dosimeters

Measurements were performed using Nanodot OSL dosimeters (Landauer, Inc., Glenwood, IL), which were read off-line using the MicroStar™ reader and then reset with the Pocket annihilator (both from Landauer, Inc.).

The calibration process described in Section II B 2 was used for the [72, 120] kVp range.

A Farmer type ionization chamber (0.6 cc, PTW 30013) was used to perform the reference dosimetry, which was itself calibrated in air-kerma in an accredited dosimetry calibration laboratory (Laboratoire National Henri Becquerel, Gif-sur-Yvette, France).

As the incident beam quality (Q) is needed in Equation (3), the spectrum was extracted from the SpekCalc software[38] after including all X-ray tube details (anode angle, inherent filtration, high voltage, additional filtration). Mass energy absorption coefficients from the NIST Standard Reference Database 126[39] were used to calculate energy absorption coefficient ratio integrated over the beam energy spectrum.

By comparing the air kerma measured by our reference ionization chamber to the calibrated OSLs as a function of depth in a homogeneous poly(methyl methacrylate) (PMMA) phantom, the maximum discrepancy in a [0, 20] cm range of PMMA was 6.9 % at a 20 cm depth. In the following we will assume $f_{Q,Q'} = 1$ while taking it into account as an additional measurement uncertainty using the 6.9 % value as our confidence interval, which translates to an expanded uncertainty (with a coverage factor[40] of $k = 2$) of 8.0 %.

Using manufacturer confidence intervals, the overall OSL measurement expanded uncertainty ($k = 2$) was estimated at 11 %. Calculations are detailed in Table IX in Appendix A and used the GUM guidelines[40].

2. Dosimetry verification phantoms

Following Damet *et al.*[12], two OSL-instrumented anthropomorphic phantoms were used: a 5 years old pediatric phantom and a female adult phantom. Each phantom is made of tissue equivalent plastic slates of 2.5 cm corresponding to either soft tissue, spinal cord or disks, lung, brain or bones ("Adult Bone" for Adult phantom, "5yrBone" for pediatric).

The 5 years old pediatric phantom (CIRS, ATOM 705, Cirs Inc., Norfolk, VA) is made of 26 plates from the head to the pelvis. Each measurement used 53 OSL Nanodot detectors placed inside the phantom.

TABLE I. Phantom hole IDs where OSL dosimeters were placed (for more details, see the documentation of the CIRS ATOM phantoms).

Tissue	Phantom hole ID (child)	Phantom hole ID (female adult)
Brain	4–7	4–7
Eyes	15, 16	16, 17
Thyroid	22, 23	26, 27
Lungs	28, 29, 53, 56, 70, 74	34, 35, 52, 56, 75, 81
Breast	58, 59	83, 84
Oesophagus	35	41, 92
Liver	105, 121, 122, 138	122, 132, 134, 136, 140
Bladder	158, 170	191, 193–195
Gonads	160, 161, 177, 178	219, 242
Stomach	101, 110	223, 224
Intestine	142–144	127, 128
Red Bone Marrow	9, 10, 17, 19, 20, 21, 38, 51, 76, 175, 176	8, 10, 20, 21, 24, 42, 162, 245, 246
Remainder tissues	61, 78, 112, 113, 115, 118, 119, 134, 159, 165	83, 84, 116, 117, 127, 128, 164, 167, 168, 177, 218, 229

The female adult phantom (CIRS, ATOM 702, Cirs Inc., Norfolk, VA) is made of 38 plates from the head to the pelvis. Each measurement used 50 OSL nanodots detectors placed inside the phantom.

The full list of OSL locations, in terms of phantom hole indices, is given in Table I.

3. Compared systems and acquisition parameters

a. DR: Fuji Visionnary DRF The DR images were acquired in a Fuji Visionary DRF radiography room (Fujifilm, Tokyo, Japan). The DR system is capable of stitching, enabling the acquisition of Full-Spine images. Female and pediatric phantoms were imaged successively using "Full Spine" and "Full Spine lateral" protocols. AP images were repeated 12 times for each phantom in order to increase signal-to-noise ratios in the OSLs, by reaching at least cumulated dose values of 0.1 mGy in the OSLs. Due to the vertical Field of View (FOV) size with respect to the detector size (43 cm × 43 cm), for each phantom and for each plane (Frontal and Lateral view), 3 images were taken and stitched together by the system. The 3 shots are referred to as 'Upper image', 'Middle image', 'Lower image'. Table II summarizes the used acquisition parameters for the DR system. The source-to-detector distance is referred to as SDD. All DR acquisitions were performed with a focused antiscatter grid.

b. Slot-scanning system: EOSedge The slot-scanning system is the EOSedge system[8], whose Flex Dose feature implements the AEC described in Section II A. The acquisition was performed using the Full-Spine low-dose protocol, in Flex Dose mode. Two patient positions were studied. Phantoms were placed in Antero-Posterior (AP) position, meaning that they were facing the frontal X-ray tube, with the lateral X-ray tube on their left. Postero-Anterior (PA) position acquisitions were also performed in order to study organ dose sparing. In PA position, phantom backs were facing the frontal tube, with the lateral tube on their right.

FIG. 1. Pediatric phantom set-up photo in the EOSedge. Phantom is in AP position. Upper slices of the phantom were removed to reveal the position of 6 OSL dosimeters in the brain. The corresponding hole index positions are shown on the schematic (top right).

The setup is shown on the pediatric phantom in FIG. 1. Images were repeated 20 times for each phantom in order to increase signal-to-noise ratios in the OSLs, by reaching at least cumulated dose values of 0.1 mGy in the OSLs. Prior to these repeated acquisitions, one scout view was acquired. Its dose contribution was found to be negligible compared to the cumulated dose of the repeated images. The overall acquisition parameters are presented in Table III.

Results were compared against reference organ dose

TABLE II. Parameters used on the Fuji Visionnary DRF for Full-Spine imaging on the pediatric and adult anthropomorphic phantoms. The inherent X-ray tube filtration was 1 mm of aluminium.

Phantom	View	kVp	Spectral filtration (mm Cu)	mA	Image before stitching	Exposure time (ms)	FOV (cm×cm)	SDD (mm)	DAP (mGy.cm^2)	Detector Dose (mGy)
Pediatric	Frontal	72	0.1	200	Upper	10	43 × 43	1500	110.4	0.06
					Middle	24			178.6	0.097
					Lower	21			167.5	0.091
	Lateral	75			Upper	14			107.5	0.058
					Middle	22			200.2	0.108
					Lower	46			397.7	0.215
Adult	Frontal	75		320	Upper	32			407.0	0.22
					Middle	53			729.6	0.395
					Lower	82			1088.2	0.589
	Lateral	80			Upper	24			300.4	0.162
					Middle	37			607.1	0.328
					Lower	158			2535.2	1.371

TABLE III. EOSedge Full-Spine low-dose protocol with Flex Dose acquisition parameters (and their scout view counterparts). The inherent X-ray tube filtration was 2.5 mm of aluminium.

Phantom	View	kVp	Spectral filtration (mm Cu)	mA	Scan speed (mm/s)	FOV (cm×cm)	SDD (mm)	DAP (mGy.cm^2)	Detector Dose (mGy)
Pediatric	Frontal	70 (120)	0.1 (2.0)	[12–55] (10)	162.5 (325)	51.4 × 67	1300	48.9 (2.7)	0.014
	Lateral	70 (120)	0.1 (2.0)	[10–100] (10)				73.2 (2.7)	0.021
Adult	Frontal	90 (120)	0.1 (2.0)	[10–30] (10)	81.25 (325)	51.4 × 115		169.9 (4.7)	0.029
	Lateral	120 (120)	0.1 (2.0)	[10–246] (10)				902.5 (4.7)	0.152

values of Damet *et al.*[12] and Pedersen *et al.*[13], measured on an EOS-1st generation system using the Full-Spine low-dose protocol.

D. Image quality assessment

1. Challenges of quantitative metrics across modalities

End-user images coming from various imaging modalities are subject to nonlinear image processing steps (including contrast enhancement and denoising steps). Hence, special attention should be paid to the selection of comparable image quality metrics. Standard metrics such as the modulation transfer function (MTF), the normalized noise power spectrum (NNPS), and the detective quantum efficiency (DQE)[41], do not account for some sources of variations in image quality, such as system magnifications, focal spot blurs, scattered radiations, and scatter rejection or correction methods, which greatly vary from one imaging modality to the other. Although the effective detective quantum efficiency[42–44] (eDQE) compensates for these shortcomings, its computation is still not suitable to compare end-user, fully processed images.

In particular, differences in the involved physical and digital imaging chains may result in different end-user image dynamic range values, that may be compensated through linear windowing operations. Hence, it is desirable that evaluated metrics be normalized with respect to gray value distributions.

2. Quantitative evaluation

In order to compare images from different imaging modalities, a normalization by an estimation of the image dynamic range, denoted Δq, is needed. When all images are encoded with the same bit depth, Δq is defined as follows. Consider a quality assurance phantom with a radio-opaque and a radio-transparent insert, and select a region of interest (ROI) in each insert. The mean light gray levels in the ROI of the radio-opaque insert, denoted v_l, and the mean dark gray levels in the ROI of the radio-transparent insert, denoted v_d, can be used to compute $\Delta q = |v_l - v_d|$. Moreover, if $v_{\max}$ is the maximum admissible value according to the image bit depth, one can compute a *normalized dynamic range* metric as:

$$\mathrm{DYN} = \frac{\Delta q}{v_{\max}}. \tag{6}$$

As suggested in Section II D 1, linear brightness and contrast adjustments are applied to the images for a fair image quality comparison. We define this operation as

follows, for an input image X:

$$W_B(X) = \text{mean}_B(X_0) + \frac{\Delta q_0}{\Delta q}\left(X - \text{mean}_B(X)\right), \quad (7)$$

where X_0 is a reference image, with dynamic range Δq_0. Mean values are computed over a certain ROI B. The following image quality metrics are computed on such transformed images.

Image noise, computed as the standard deviation of a transformed image $W_{B_0}(X)$ in a homogeneous region B_0, is defined as:

$$\sigma_{B_0}(W_{B_0}(X)) = \frac{\Delta q_0}{\Delta q}\sigma_{B_0}(X). \quad (8)$$

Due to the contrast adjustment performed by operator $W_{B_0}(\cdot)$, it is a scaled version of the original image noise $\sigma_{B_0}(X)$.

The *signal-to-noise ratio (SNR)* of image $W_{B_0}(X)$ is also defined as:

$$\text{SNR} = \frac{\text{mean}_{B_0}(W_{B_0}(X))}{\sigma_{B_0}(W_{B_0}(X))} = \frac{\Delta q}{\Delta q_0}\cdot\frac{\text{mean}_{B_0}(X_0)}{\sigma_{B0}(X)}. \quad (9)$$

Note that since image mean values have been centered to $\text{mean}_{B_0}(X_0)$, the SNR is inversely proportional to the noise metric.

In order to account for differences in SNR values due to changes in exposure between imaging systems, the *SNR-to-dose ratio* (SNRD) is also computed as[45]:

$$\text{SNRD} = \frac{\text{SNR}}{\sqrt{D_{\text{det}}}}, \quad (10)$$

where D_{det} is the detector dose. The higher the SNRD, the better the tradeoff between the SNR and the dose.

Contrast metrics are not impacted by the brightness/contrast transformations; in particular, the *contrast-to-noise ratios* (CNR) are defined as:

$$\text{CNR} = \frac{|\text{mean}_C(W_B(X)) - \text{mean}_B(W_B(X))|}{\sigma_B(W_B(X))} \quad (11)$$

$$= \frac{|\text{mean}_C(X) - \text{mean}_B(X)|}{\sigma_B(X)}, \quad (12)$$

where C is a small ROI in the contrasted region, and B is a small ROI in the surrounding background near C.

Optimizing the CNR does not account for potential dose increase. In order to account for differences in CNR values due to exposure changes, the *CNR-to-dose ratio* (CNRD) is also computed as[46–48]:

$$\text{CNRD} = \frac{\text{CNR}}{\sqrt{D_{\text{det}}}}. \quad (13)$$

Note that the CNRD is independent of the mAs. The higher the CNRD, the better the tradeoff between contrast performances and dose.

3. Qualitative evaluation

Quantitative image quality metrics do not fully capture all the criteria that make an end-user image usable or not for given clinical applications. In addition to quantitative evaluations, qualitative evaluations, based on at least two human observers, are also recommended[9,49,50]. For a fair comparison, images should be properly windowed in order to get a similar dynamic range in all tested modalities. Visual criteria generally include a list of anatomical structures, and experts either score images according to a given scale, or arrange the reviewed images in the order of preference[49]. Qualitative image quality evaluations are performed on anthropomorphic phantoms, or directly on clinical data.

E. Image quality experiments & set-up

Two types of assessments were carried out: *(i)* a quantitative image quality assessment on a quality assurance phantom, and *(ii)* a qualitative assessment on an anthropomorphic phantom as well as on clinical images.

All the image quality analyses were performed on end-user images, that were processed by various (possibly non-linear) image processing steps. All images were encoded as 16-bit images and compared as such.

1. Quantitative evaluation

A fluoro quality test phantom (PHD5000, Varay Laborix, Bourges, Belgium) was used to compare image quality metrics across the tested modalities (FIG. 2). It consists of a 9 mm thick acrylic disk, that embeds high-resolution pattern ranging from 0.5 to 5 line pairs per millimeter (lp/mm), a radio-opaque and a radio-transparent insert, and a collection of low-contrast inserts with relative contrast values ranging from 0.3 % to 13.2 %. The PHD5000 phantom was imaged behind 10 cm, 20 cm, 30 cm, and 40 cm of PMMA, in order to assess tested metrics under conditions with different attenuations. Acquisitions were performed in frontal view only, with the phantom adjacent to the image receptor, on the EOS-1$^{\text{st}}$ generation system, the EOSedge system, and the DR system, for all four tested PMMA thicknesses. On the EOS-1$^{\text{st}}$ generation system, the constant exposure parameters were used from default tables. The EOSedge system used the Flex Dose option; since the attenuation does not vary much over the vertical field of view, the mA profile was almost constant. On the DR system, images were acquired using a Localized protocol, with default exposure parameters, using the same focused antiscatter grid for all acquisitions. Acquisition parameters are summarized in Table IV.

In addition to the detector dose values for each acquired image, the following image quality metrics were

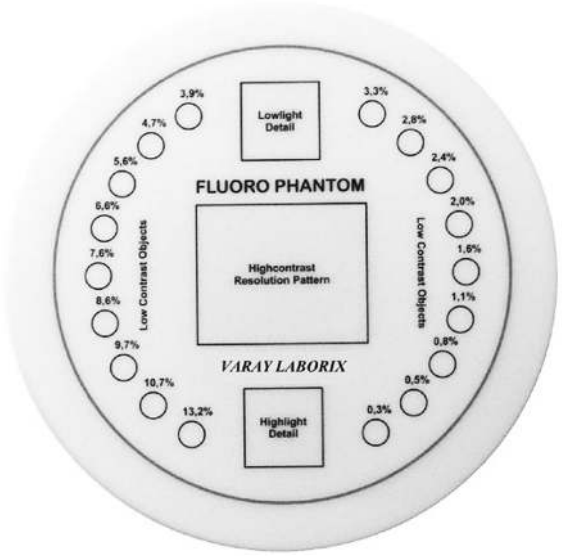

FIG. 2. The PHD5000 fluoro quality test phantom.

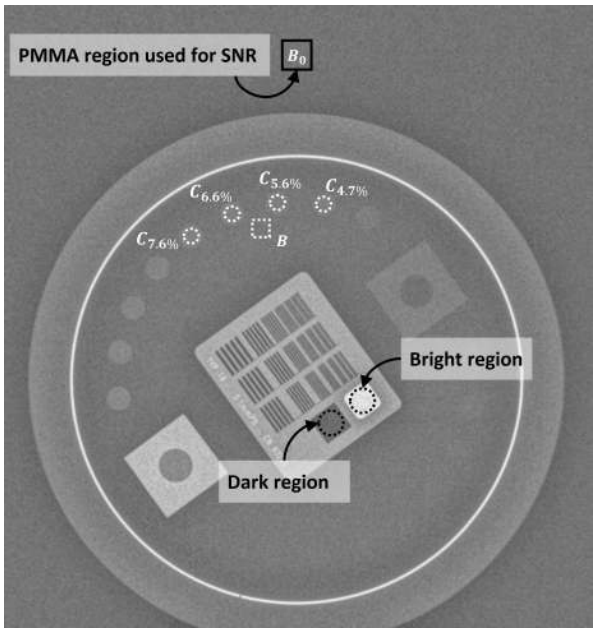

FIG. 3. Image of the PHD5000 phantom imaged on EOSedge behind 20 cm of PMMA; the regions of interest used to compute image quality metrics are displayed on the image.

computed on this phantom, using the different regions of interest (ROI) displayed on FIG. 3:

The dynamic range was used to measure how well gray levels are distributed over the available bit depth. The dark and light regions, displayed as black dotted circles on the radio-opaque and radio-transparent inserts, were used to compute the mean dark gray and light gray values, denoted v_d and v_l, respectively; they are used to compute the normalization factor Δq as well as the normalized dynamic range metric DYN according to Equation (6).

The spatial resolution was estimated by reading the high-contrast resolution pattern; the detectable high-resolution pattern with the highest line pairs per millimeter gives the spatial resolution of the image. The higher the metric, the better the spatial resolution.

The low-contrast resolution was estimated by visually assessing which low-contrast inserts could be detected, and translating these assessments into the corresponding relative contrast values (see FIG. 2). The smaller the detected relative contrast, the better the low-contrast resolution.

The image noise is estimated from a small region B_0 in the PMMA (displayed as a black square in FIG. 3), using Equation (8) with the previously computed normalization factor Δq. Noise was computed on the brightness- and contrast-adjusted images derived from Equation (7), using the EOSedge images as the reference images.

The signal-to-noise ratio (SNR) was computed using Equation (9) with the previously computed image noise metric. The SNR was computed on the brightness- and contrast-adjusted images derived from Equation (7), using the EOSedge images as the reference images.

The SNR-to-dose ratio was computed using Equation (10) with the previously computed SNR.

Contrast-to-noise ratios were computed on contrast inserts with relative contrasts X, where $X \in \{7.6\%, 6.6\%, 5.6\%, 4.7\%\}$. For each of these contrasts, a small circular ROI within the insert (denoted C_X in FIG. 3) was used to compute the CNR with respect to a small region B in the PHD5000 phantom near the tested inserts, according to Equation (12).

CNR-to-dose ratios were also computed, using Equation (13) with the previously computed CNR metrics.

2. Qualitative evaluation

The image quality performance of EOSedge with respect to the EOS-1st generation and the DR system was also qualitatively assessed. When compared, images were properly windowed. Images were reviewed by two independent image quality experts, with respect to five visual criteria: the detectability of vertebral bodies, pedicles, transverse processes, and spinous processes, following the

TABLE IV. Acquisition parameters for quantitative image quality assessment on the PHD5000 phantom; parameters are provided for PMMA thicknesses [10 cm, 20 cm, 30 cm, 40 cm]. The inherent X-ray tube filtration was 2.5 mm of aluminium for both EOS-1st generation and EOSedge, and 1 mm for the Fuji Visionary DRF system. For EOSedge, the mean tube current value is shown.

Imaging system	kVp	Spectral filtration (mm Cu)	mA	Exposure time (s)	FOV (cm×cm)	SDD (mm)
EOS-1st generation	[83–90–100–100]	0.1	[200–250–250–250]	[4.4–4.4–4.4–4.4]	45 × 33	1300
EOSedge	[60–90–120–120]		[88–182–247–349]	[1.0–1.0–2.5–8.1]	51 × 33	1300
Fuji Visionary DRF	[60–75–115–120]		[250–320–500–500]	[0.8–1.4–0.7–2.8]	43 × 43	1500

choices of Yvert *et al.*[9], based on a simple two-scale rating (feature can be detected or not); and the perceived image noise consistency in connection with the tube current modulation. Dose values were also compared, in order to give a sense of the image quality/dose tradeoff.

a. EOS-1st generation vs. EOSedge In order to check the impact of Flex Dose on image quality, the anthropomorphic RANDO® phantom (Radiology Support Devices, Inc., Long Beach, CA) was harnessed and suspended vertically, so that it could be imaged in both the EOS-1st generation system, which keeps the exposure constant along the scan, and the EOSedge system, with Flex Dose. The RANDO phantom represents an average-size man, with a natural human skeleton; contrary to the CIRS phantoms used for dose measurements, it is very well adapted to qualitative evaluations of image quality. Its morphotype is also very close to the morphotype of the adult female phantom.

Both systems used their own Full-Spine low-dose protocols, with Flex Dose for EOSedge. The overall acquisition parameters are presented in Table V. Produced images were visually compared with respect to the five criteria listed previously.

b. DR vs. EOSedge In order to compare EOSedge image quality against DR, clinical images from a group of three patients who underwent both localized DR exams using the very same Fuji Visionnary DRF system as in the dose study, and a biplanar Full-Spine low-dose (with Flex Dose) acquisition on EOSedge, were used (Table VI). Patients were extracted from a database of previously collected clinical images, and images in both modalities may not have been acquired the very same day. Localized DR images focused either on the cervical spine (CSPINE), the thoracic spine (TSPINE) or the lumbar spine (LSPINE), and these regions were compared to their EOSedge counterparts. The DR detector dose values were computed using Equation (14a):

$$D_{\text{det}} = \frac{\text{DAP}}{\mathcal{A}}, \tag{14a}$$

where DAP is the detector dose-area product and $\mathcal{A}$ is the exposed detector area. The detector dose values corresponding to the studied cropped regions from the EOSedge Full-Spine images needed an additional scaling factor corresponding to the ratio of the mean tube current value in the cropped region over the mean tube current value of the whole scan:

$$D_{\text{det}} = \frac{\text{DAP}}{\mathcal{A}} \times \frac{\text{mean}_{\text{ROI}}(\text{mA})}{\text{mean}(\text{mA})}. \tag{14b}$$

In Equation (14b), DAP is the detector dose-area product of the Full-Spine acquisition and $\mathcal{A}$ is the Full-Spine exposed area in the detector plane. We call "regions of interest" (ROI), the DR localized exposed detector areas, or the corresponding cropped regions of the EOSedge Full-Spine images.

III. RESULTS

A. Dose comparison

1. Pediatric Phantom

The organ doses measured in the pediatric phantom in the three tested systems are gathered in FIG. 4. All organ doses were under 0.1 mGy for EOSedge, and under 0.7 mGy for DR. Organ dose to the thyroid varies from 19 μGy in EOSedge, and 267 μGy in the DR system. Dose to the breast is 0.033 μGy in the EOSedge, and 0.189 μGy in the DR system.

Effective doses were calculated for the child phantom, and gathered in Table VII. Dose ratios were computed against EOSedge as a reference. Effective doses range from 32 μSv for a Full-Spine scan in EOSedge to 179 μSv for the DR system. Effective dose reference values for the same pediatric phantom on EOS-1st generation were 200 μSv[12] and 196 μSv[13].

As patient positioning was studied in AP and PA in the EOSedge system, organ dose measurements were subdivided into left and right parts when possible (FIG. 5).

2. Female adult phantom

The organ doses measured in the female adult phantom in the three tested systems are gathered in FIG. 6. For EOSedge the organ doses range from 42 μGy in the T/L-Spine to 1.15 mGy in the femurs. For the DR system, the lowest dose was measured in the brain with 134 μGy,

TABLE V. EOS and EOSedge (with Flex Dose) Full-Spine low-dose protocol acquisition parameters for the RANDO phantom. For EOSedge, the dose-area product (DAP) values cumulate the scout view DAP and the image DAP. The inherent X-ray tube filtration was 2.5 mm of aluminium for both systems.

Imaging system	View	kVp	Spectral filtration (mm Cu)	mA (mean)	Scan speed (mm/s)	FOV (cm×cm)	SDD (mm)	DAP (mGy.cm^2)	Detector dose (mGy)
EOS-1st generation	Frontal	90	0.1	250	76	91 × 45	1300	351.4	0.09
	Lateral	105		250				534.0	0.13
EOSedge	Frontal	90		[10–57] (34)	108.33	96 × 51		236.7	0.05
	Lateral	120		[10–232] (41)				457.1	0.9

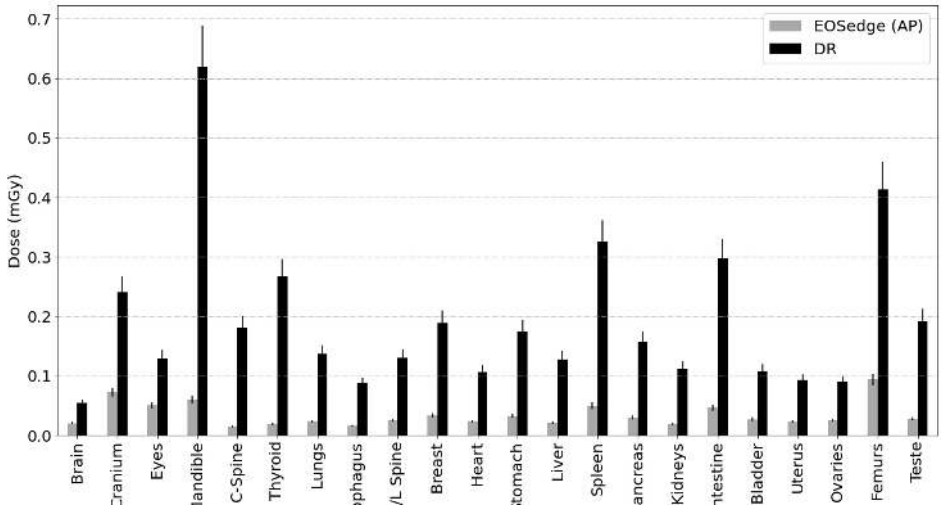

FIG. 4. Organ dose measurements for the pediatric phantom (mean dose per organ computed as the average of dose measures in the OSLs) in the EOSedge and DR systems in AP patient position. Error bars are given at $k = 2$, following Section II C 1.

TABLE VI. Description of the three clinical cases

Anatomy	CSPINE	TSPINE	LSPINE
Sex	F	F	M
Age	32	21	36
Height (m)	1.63	1.75	1.74
Weight (kg)	55	62	80

while the highest one was measured in the femurs with 1.42 mGy.

As performed for the pediatric phantom, effective doses were calculated for the female adult phantom. Results are shown in Table VII, and calculations are detailed in Table XI in Appendix B. Effective doses range from 92 μSv for a Full-Spine scan in EOSedge to 572 μGy in the DR system. Reference value for EOS-1st generation in the literature were 290 μSv[12] and 220 μSv[13].

Adult organ dose deposition results for both patient orientations in EOSedge are gathered in FIG. 7. Dose to right eye is 86 μGy in AP, 50 μGy in PA. On the left eye, dose is 119 μGy in AP, 41 μGy in PA. Dose to the right ovary, (respectively left ovary) were 81 μGy, (resp. 236 μGy in AP position), and 272 μGy, (resp. 82 μGy in PA position).

B. Image quality

1. Quantitative evaluation

The detector dose, the image noise values, the SNR values, and the SNRD values are shown in FIG. 8. Both EOS-1st generation and the DR systems show an increasing noise with PMMA thicknesses; in contrast, the noise metric remains fairly stable for EOSedge: it is above EOS-1st generation and DR for attenuations lower than 30 cm of PMMA, but below them at 30 cm and 40 cm of PMMA (FIG. 8(b)). On the contrary, EOS-1st generation and the DR systems show decreasing trends in SNR with PMMA thicknesses; EOSedge, however, shows a more stable trend with PMMA thicknesses, at a medium level (FIG. 8(c)). In terms of SNRD, EOS-1st generation outperforms the other tested systems, with EOSedge being a compromise between EOS-1st generation and the

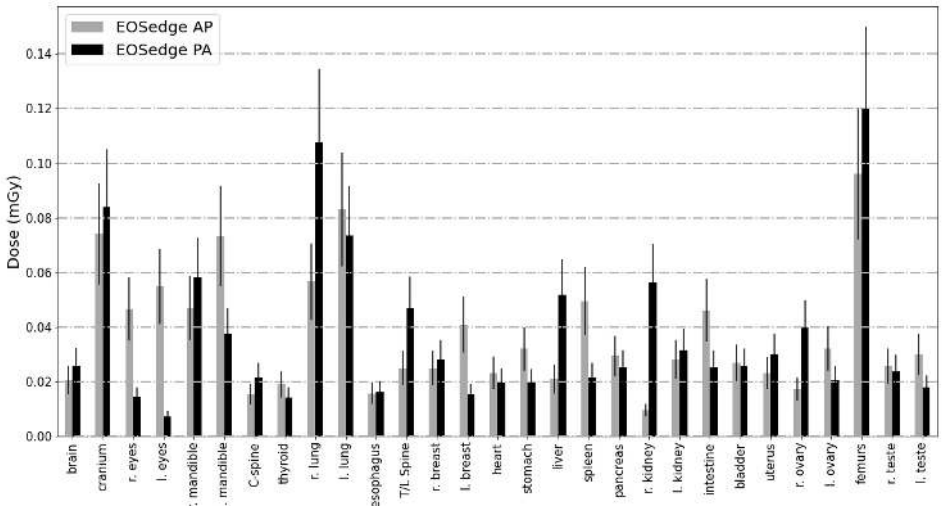

FIG. 5. Organ dose measurements for the pediatric phantom (mean dose per organ computed as the average of dose measures in the OSLs) in the EOSedge system in AP patient position and in PA patient position. Error bars are given at $k = 2$, following Section II C 1.

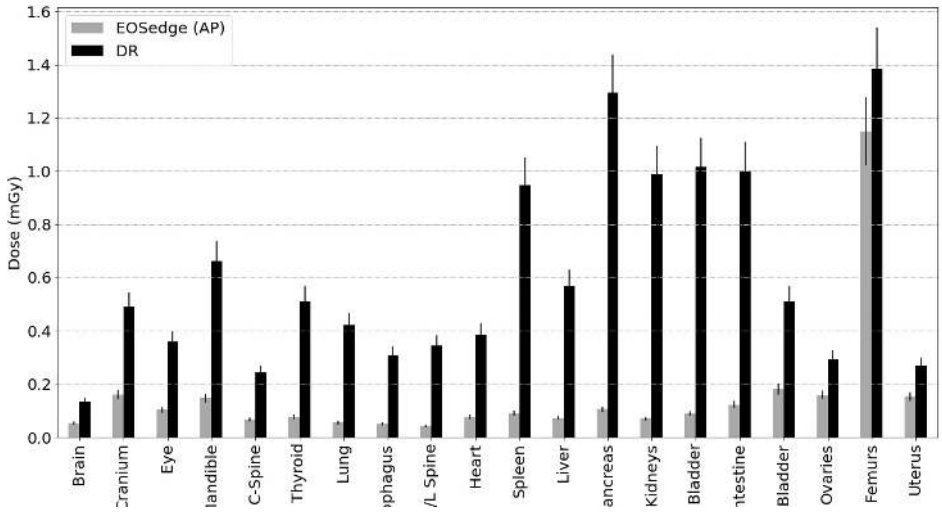

FIG. 6. Organ dose comparison for the female adult phantom (mean dose per organ computed as the average of dose measure in the OSLs) in the DR and EOSedge system in AP patient position. Error bars are given at $k = 2$, following Section II C 1.

DR system (FIG. 8(d)).

These observations need to be weighted against other image quality metrics, such as those shown in FIG. 9. Both the EOS-1st generation and the DR systems show a decreasing trend in terms of image dynamic range (DYN) as the PMMA thickness increases; EOSedge, however, shows a stable dynamic range (DYN) across the tested PMMA thicknesses, at a reasonable level between 40 % and 50 % (FIG. 9(a)). In terms of spatial resolution, all the tested systems show a decreasing trend as the PMMA thickness increases (FIG. 9(b)). With larger pixel sizes than the other systems, the curve of EOS-1st generation decreases from 2 lp/mm for 10 cm of PMMA, to 0.5 lp/mm for 40 cm of PMMA. In contrast, both EOSedge and the DR systems provide a spatial resolution up to 3.55 lp/mm for 10 cm and 20 cm of PMMA; however, for larger PMMA thicknesses, EOSedge better preserves spatial resolution (down to 2.8 lp/mm) than the DR system (down to 1.8 lp/mm). The rates of spatial resolution loss with increasing PMMA thicknesses

TABLE VII. Effective dose comparison according to the definition of the ICRP[37]

		Effective dose (mSv)	Ratio (modality/EOSedge)
Pediatric phantom	DR	0.179	5.6
	EOS-1st generation[12]	0.2 (0.196)	6.2 (6.1)
	([13])		
	EOSedge AP	0.032	1
Female adult phantom	DR	0.572	6.2
	EOS-1st generation[12]	0.29 (0.22)	3.1 (2.4)
	([13])		
	EOSedge AP	0.092	1

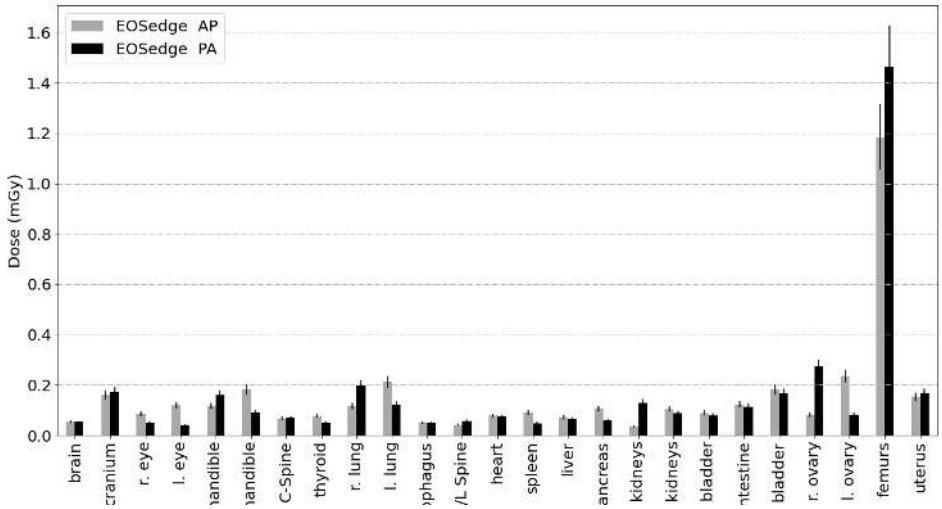

FIG. 7. Organ dose measurements for the female adult phantom (mean dose per organ computed as the average of dose measures in the OSLs) in the EOSedge system in AP patient position and in PA patient position. Error bars are given at $k = 2$, following Section II C 1.

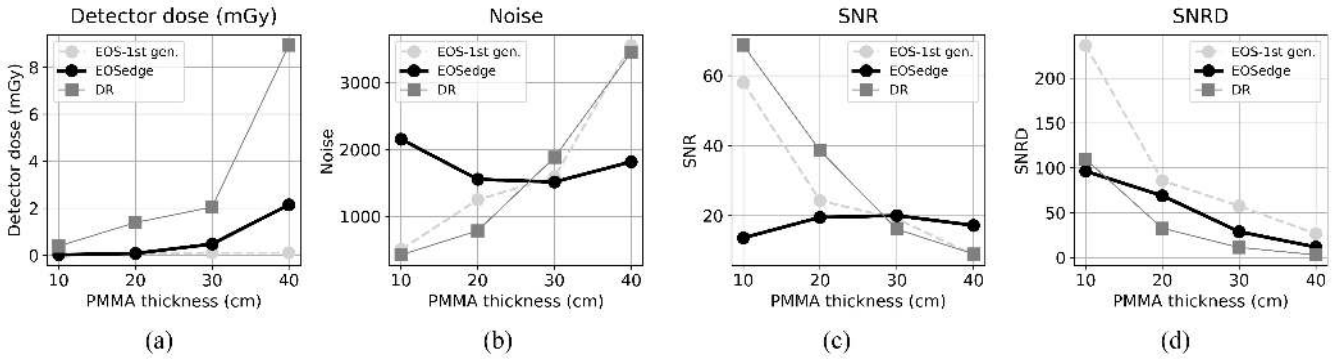

FIG. 8. Dose and noise metrics on the PHD5000 phantom as a function of the attenuation. (a) Detector dose. (b) Noise. (c) SNR. (d) SNR-to-dose values.

correlate with the noise values from FIG. 9(b).

Moreover, in terms of low-contrast detection (FIG. 9(c)), EOS-1st generation quickly misses the inserts with small relative contrast values; EOSedge and the DR systems behave similarly for 10 cm and 20 cm of PMMA, but EOSedge still detects relative contrasts as

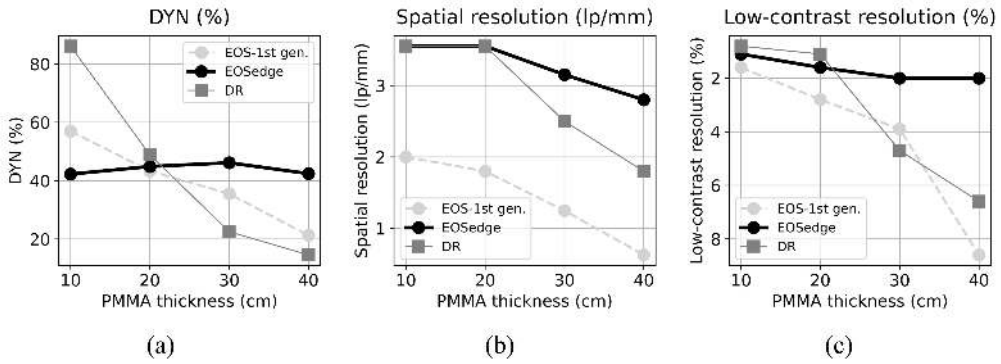

FIG. 9. Global image quality metrics on the PHD5000 phantom as a function of the attenuation. (a) Dynamic range metric. (b) Spatial resolution metric. (c) Low-contrast resolution metric.

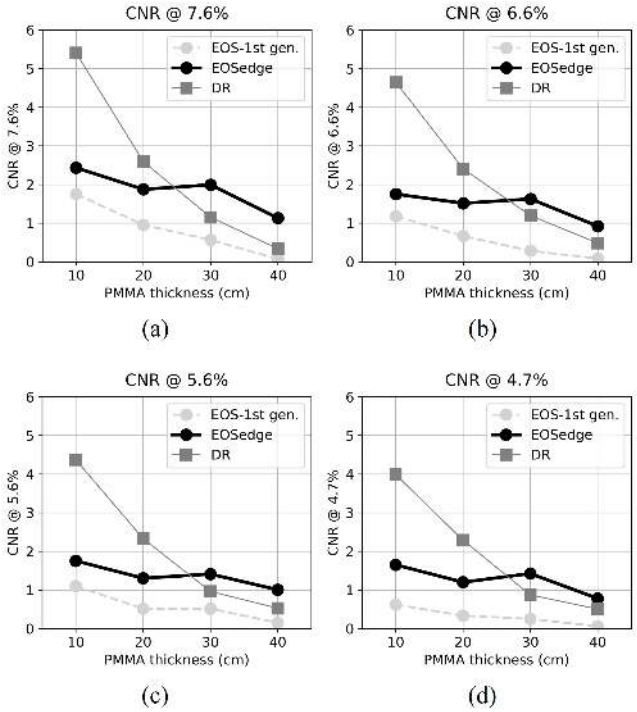

FIG. 10. CNR curves as a function of attenuation in four low-contrast inserts of the PHD5000 phantom. (a) 7.6% relative contrast insert. (b) 6.6% relative contrast insert. (c) 5.6% relative contrast insert. (d) 4.7% relative contrast insert.

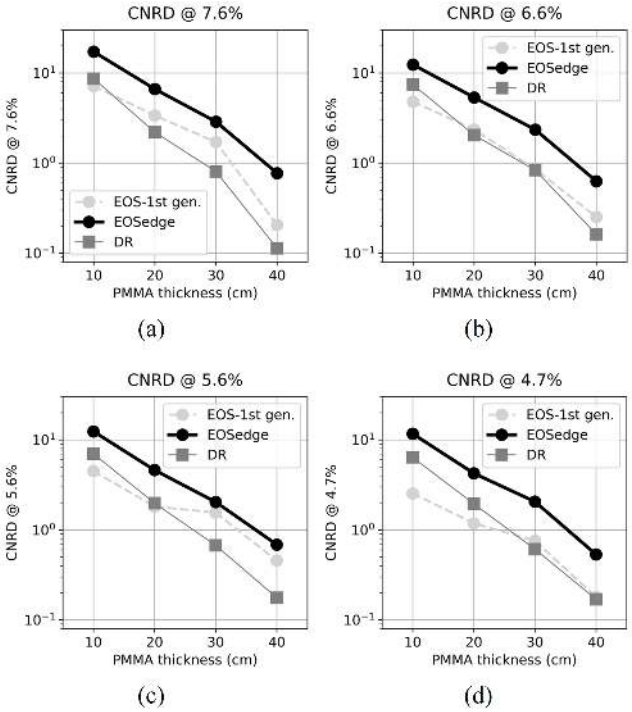

FIG. 11. CNR-to-dose ratios (CNRD) as a function of attenuation in four low-contrast inserts of the PHD5000 phantom. (a) 7.6% relative contrast insert. (b) 6.6% relative contrast insert. (c) 5.6% relative contrast insert. (d) 4.7% relative contrast insert.

low as 2 % for 40 cm of PMMA, whereas inserts in the DR image can only be detected down to 8.6 %.

The CNR values for the four tested contrast inserts are shown in FIG. 10. EOS-1st generation has the poorest CNR scores, with CNR values always lower than 2, down to less than 0.1. DR images show excellent CNR values at low PMMA thicknesses, but they drop at 30 cm and 40 cm of PMMA. EOSedge shows a more stable behavior, with CNR values almost always greater than 1 and up to 2.4, at a level where detection is possible. Note that low-contrast inserts with CNR values lower than 0.5 cannot be visually detected, even with narrowed display windows.

The CNRD values for the four tested contrast inserts are shown in FIG. 11. They show that EOSedge provides

the best tradeoff between CNR performance and dose, for all the tested inserts, at all the tested PMMA thicknesses.

2. Qualitative evaluation

a. EOS-1st generation vs. EOSedge Acquired images for the EOS-1st generation vs. EOSedge image quality comparison are shown in FIG. 12. The tube current profiles from the Flex Dose show how the mA changes along the scan. As expected, on the frontal view, the tube current values were lower in the cervical area (around 10 mA), while they increase in the skull and in the pelvis, up to a factor 5.7. The impact of tube current modulation is even more prominent in the lateral view, where values can increase up to a factor 23. In particular, the dose can locally increase in the pelvic area and in the shoulders, where attenuation was much greater.

Detailed side-by-side comparisons are displayed in FIG. 13. FIGs. 13(a) and 13(c) display comparisons of the frontal images in both the upper thoracic and lumbar areas. Interestingly, the perceived noise level is visually equivalent in both regions on the EOSedge zoomed images (right), despite a mean tube current ratio of approximately 4 between the two exposed regions. The visibility of the vertebral bodies, pedicles, transverse processes, and spinous processed, is similar in both the EOS-1st generation zoomed images (left) and the EOSedge images (right).

Similarly, FIGs. 13(b) and 13(d) display comparisons of the lateral images in both the cervico-thoracic junction, and the lumbar and pelvic areas. The observation regarding image noise still holds, with this time mA values jumping from around 10 mA in the cervico-thoracic junction, to 232 mA in the pelvis. As for the frontal images, all the landmarks of interest that were detectable on EOS-1st generation zoomed images (left) can also be detected on the EOSedge images (right).

The entrance dose values at 15 cm from the isocenter are summarized in Table V. They show that compared to EOS-1st generation, EOSedge provided an entrance dose reduced by 46 % in the frontal view, and by 22 % in the lateral view.

b. DR vs. EOSedge The image acquisition parameters are displayed in Table VIII.

The CSPINE comparison was only available for the lateral view. The DR image and the corresponding EOSedge image crop are displayed in FIG. 14. In this anatomical area, the tube current values remain mostly close to 10 mA, with an increase at the cervico-thoracic junction. Visually, the vertebral bodies, spinous processes, and pedicles were visible on both images.

The frontal and lateral image comparisons for the TSPINE are available in FIGs. 15 and 16, respectively. The tube current values remain quite low in this anatomical area as well, since thoracic vertebrae were mostly surrounded by air, except near the cervico-thoracic junction where the shoulder thicknesses require more exposure in the lateral view. Again, visually, the anatomical landmarks were detected in both the DR and the cropped EOSedge images, in the frontal and the lateral views.

The frontal and lateral image comparisons for the LSPINE are available in FIGs. 17 and 18, respectively. This anatomical area shows more variations in the tube current modulation profile, in both frontal and lateral views, with a more prominent effect in the lateral view. Between the DR and the cropped EOSedge images, no difference was observed in landmark detectability along the spine.

Detector dose values shown in Table VIII suggest that the EOSedge has significantly lower dose than the DR, with preserved image quality.

As can be seen in the regions of interest shown in the aforementioned figures, the tube current modulation profiles of a Full-Spine exam on EOSedge may spread from 10 mA to more than 100 mA in the frontal views and up to 350 mA in the lateral views for the studied cases. However, we visually observe no image quality drop regardless of the anatomical area. More importantly, entrance dose comparisons between the DR images and their EOSedge counterparts show a significant patient dose reduction without compromising image quality for clinical tasks such as follow-ups of spinal deformities.

IV. DISCUSSION

This study describes the first organ dose comparison between a slot-scanning system with an AEC and a DR system on CIRS ATOM phantoms. It is put in connection with image quality comparisons, quantitatively through measurements on a quality assurance phantom with varying PMMA thicknesses, and qualitatively, first between EOS-1st generation and EOSedge on the RANDO phantom, and then between DR and EOSedge on three clinical cases.

An effective dose reduction in the EOSedge was observed for both pediatric and adult phantoms, compared to the other tested system. Effective doses were about 6 times lower when comparing EOSedge to the DR exam for both phantoms. It is worth mentioning that default protocols were used on all modalities. Hence measures reflect the dose that patient would receive using the standard imaging workflows. Moreover, the stop-and-shoot behavior of the Fuji Visionnary DRF AEC was observed from the measures (FIG. 6). The AEC adapted exposure for each of the three acquired shots. As mentioned earlier, the FOV was divided into three images (Upper: Head, Middle: Thorax/Abdomen, Lower: Pelvis). One can observe that the dose to organs located in pelvic region was higher than the dose in Thoracic region. The dose to the pancreas was 4 times higher than the dose to the oesophagus (see FIG. 6). Indeed, X-ray exposure was 4 times longer in the pelvic region compared to the thoracic region on the lateral image, while it was reduced by 1.5 on the frontal exposure (Table II).

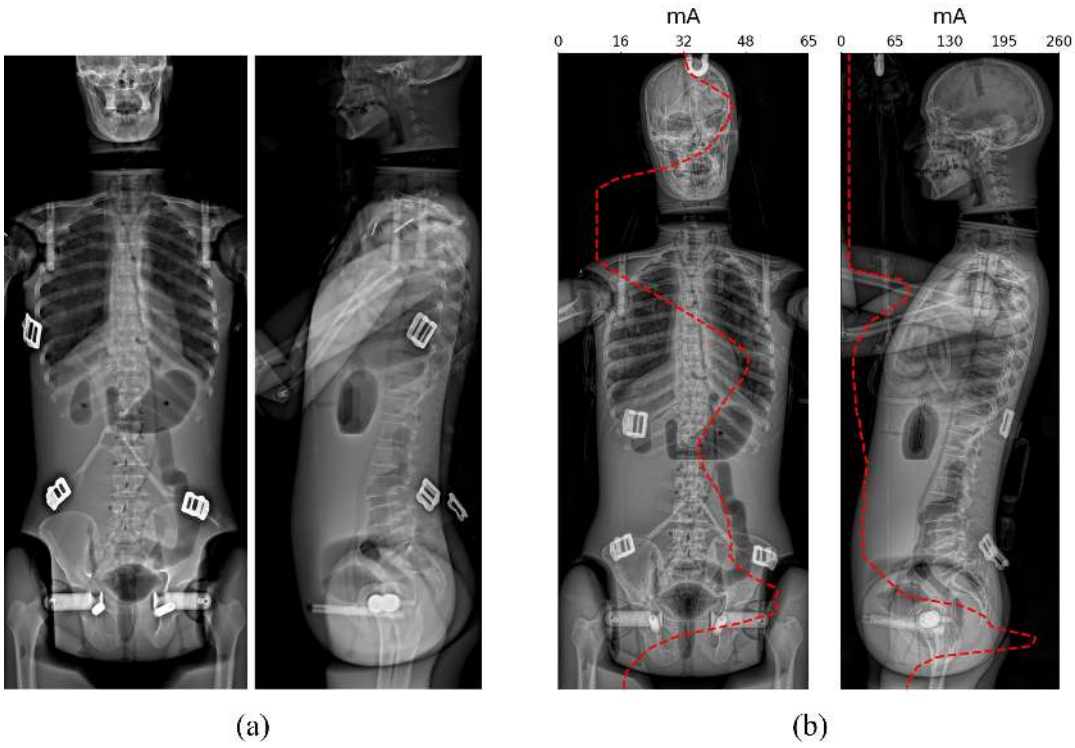

FIG. 12. (a) EOS-1st generation biplane images. (b) EOSedge biplane images. The tube current modulation profiles along the scan are superimposed to the images.

TABLE VIII. DR vs. EOSedge acquisition parameters and detector dose values, computed according to Section II E 2 b. The region-of-interest (ROI) corresponds either to the full exposed detector area for DR, or to the cropped region of the EOSedge Full-Spine image that fits the localized DR image.

Anatomy	View	kVp	mA in ROI (mean)	Speed (mm/s)	ROI Exposure time (s)	ROI FOV (cm×cm)	SDD (mm)	DAP in ROI (mGy.cm^2)	Detector dose in ROI (mGy)
CSPINE (DR)	Lateral	70	321	NA	0.096	25×12	1420	96	0.32
Full-Spine (EOSedge)	Lateral	120	[10–69] (18)	108.33	1.947	21×15	1300	12.73	0.04
TSPINE (DR)	Frontal	65	320	NA	0.074	41×14	1100	170	0.30
	Lateral	70	319	NA	0.052	41×19	1310	148	0.19
Full-Spine (EOSedge)	Frontal	90	[10–44] (35)	108.33	3.691	40×16	1300	25.53	0.04
	Lateral	120	[10–70] (24)	108.33	2.875	31×21	1300	39.54	0.06
LSPINE (DR)	Frontal	80	400	NA	0.215	42×31	1500	2874	2.1
	Lateral	105	500	NA	0.134	41×20	1250	3340	4.07
Full-Spine (EOSedge)	Frontal	100	[59–119 (83)	108.33	3.23	35×40	1300	179.65	0.13
	Lateral	120	[55–224] (142)	108.33	3.11	34×24	1300	261.08	0.32

Due to the vertical slot-scanning, EOSedge Flex Dose was designed as a continuous AEC that adapts dose at each altitude of the scan. Doses to the femurs were similar in both the EOSedge and the DR acquisitions, yet dose decreased more rapidly along the patient vertical axis (from tail to crown), as the attenuation decreases. The dose to the ovaries was 1.8 times lower in the EOSedge than in the DR (FIG. 6).

In previous studies, Damet *et al.*[12] and Pedersen *et al.*[13] estimated organ dose while performing EOS-1st generation scans. They used TLD dosimeters. In the present study, except for the dosimeter model (OSL), the measurement method was similar to these studies. Indeed, dosimeters were placed in similar organs (brain, thyroid, lungs, oesophagus, breast, stomach, liver, intestine, bladder, ovaries) on the same pediatric and female adult CIRS phantoms, for the same EOS-1st generation Full-Spine protocol.

Compared to Damet *et al.*[12] and Pedersen *et al.*[13] dose values on EOS-1st generation system, a dose reduction factors ranging from 2.4 to 3.2 for the adult phantom and about 6 for the pediatric phantom was observed

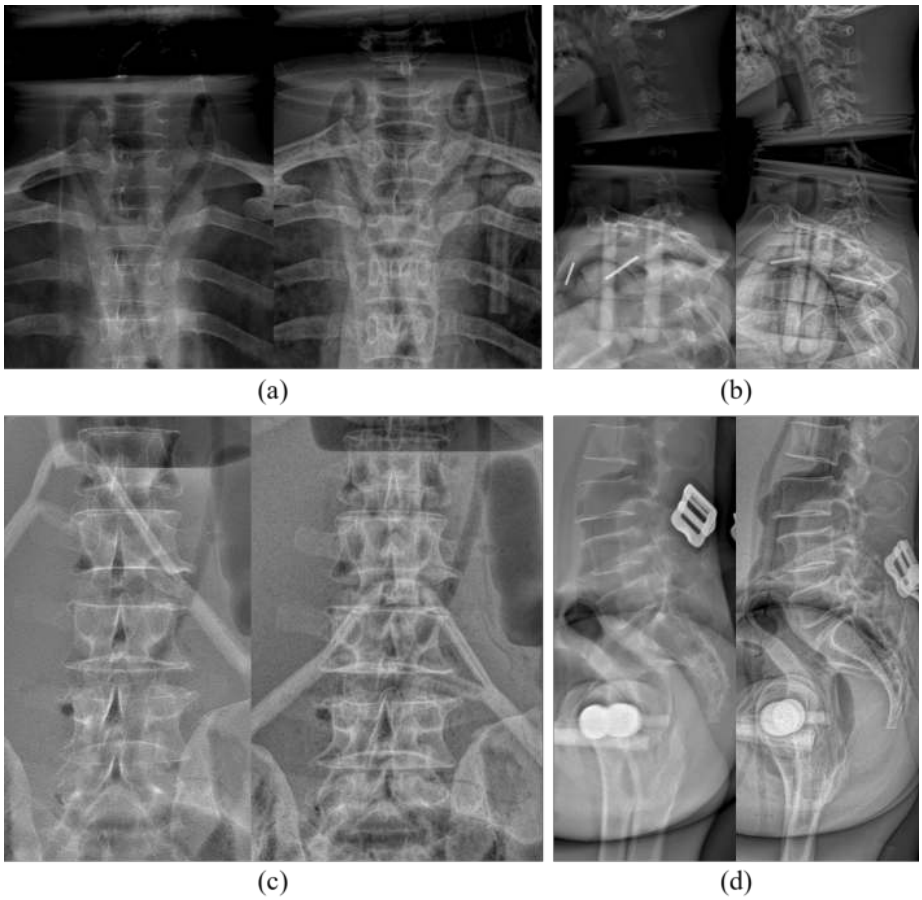

FIG. 13. Detailed side-by-side comparisons between EOS-1st generation (left) and EOSedge (right) images, for the first thoracic vertebrae in frontal view (a), the cervico-thoracic junction in lateral view (b), the lumbar vertebrae in frontal view (c) and in lateral view (d).

when using the EOSedge Flex Dose. Interestingly, EOS-1st generation acquisitions were performed with fixed mA along the vertical scan, whereas EOSedge introduced an AEC with tube current modulation. Hence, in the adult phantom, doses to the uterus were similar between EOS-1st generation[12,13] and EOSedge while dose to the lung was 4 times lower with EOSedge (see Table XI, 0.27 mGy in EOS-1st generation, 0.055 mGy in EOSedge). This confirms that EOSedge further reduces patient dose compared to its previous-generation counterpart, which was already known to be low dose[51,52]. Moreover, for the pediatric phantom, EOS-1st generation and EOSedge result in acquisition times lower than 5 seconds, making them suitable for younger pediatrics to stand still without reported motion artifact[53].

Patient positioning in the EOSedge system also plays a role in organ dose sparing. Organs facing an X-ray tube receive the highest irradiation. For instance, the use of PA positing instead of AP will have a dose sparing effect on the eyes, with a dose reduction of a factor of 2 for adults to 4 for children. Doses to the ovaries were similar in AP and PA positions with the exception of having the ovary closest to the X-ray source (left in AP, right in PA) receiving about three times more dose than the opposite one. However, these dose values remained low, below 300 μGy.

Beyond standard low-dose protocols, EOS-1st generation introduced a micro-dose protocol dedicated to patient follow-up exams[1], that further reduces patient dose. Pedersen *et al.*[13] calculated the effective dose for adult and child phantoms undergoing micro-dose exams in the EOS-1st generation. Pediatric exam using the micro-dose protocol on EOS-1st generation resulted in an equivalent effective dose (about 25 μSv) comparable to the EOSedge low-dose protocol with Flex Dose (32 μSv, see Table VII).

EOSedge also provides a micro-dose protocol combined with Flex Dose; although this protocol was not studied in this work, one can expect an additional dose reduction compared to the studied protocols.

According to the United Nations Scientific Committee on the Effects of Atomic Radiation (UNSCEAR), weekly natural background radiation is estimated around 46 μSv[54]. According to the estimated effective dose, EOSedge examinations is equivalent to 5 days of natural radiation for children and 2 weeks for adults.

Although significant cumulated dose reduction factors

FIG. 14. (a) Localized lateral DR image of a cervical spine. (b) Same area extracted from the corresponding lateral EOSedge low-dose (with Flex Dose) Full-Spine acquisition. The shape of the tube current modulation profile is shown as a dashed line.

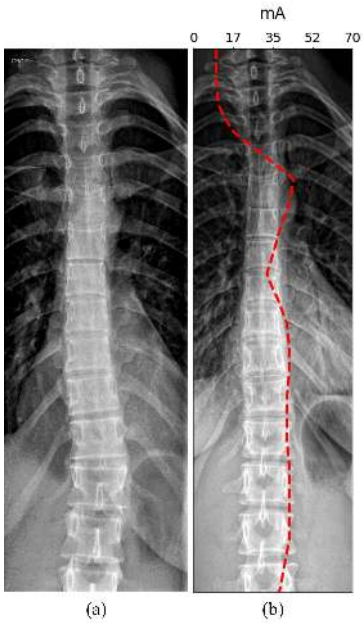

FIG. 15. (a) Localized frontal DR image of a thoracic spine. (b) Same area extracted from the corresponding frontal EOSedge low-dose (with Flex Dose) Full-Spine acquisition. The tube current modulation profile is shown as a dashed line.

were observed when moving from EOS-1st generation to EOSedge with Flex Dose, it is interesting to note the benefit of AEC even in a virtual scenario where cumulated patient exposures had been exactly the same: indeed, for the same dose, the AEC would distribute the dose less when not needed (e.g., in the cervicals), and more when necessary (e.g., in the pelvic area).

Most importantly, the dose comparison study should be looked at in relation to the image quality comparison that was done. In terms of image quality, the goal of Flex Dose was to provide a stable target signal-to-noise ratio, regardless of the attenuation; this target is set in order to reach reasonable performances in terms of spatial resolution, low-contrast resolution, and contrast-to-noise ratio, while keeping the dose low. The quantitative image quality assessment confirmed that these metrics remain much more stable with EOSedge than with the two other tested modalities, across an attenuation range from 10 cm to 40 cm of PMMA; note that this range includes both the pediatric and the female adult phantoms, whose equivalent patient thicknesses are 15 cm and 20 cm in the frontal view, and 19 cm and 34 cm in the lateral view, respectively. Small variations in the metric values may be caused by nonlinear image processing instabilities across morphotypes. Among the studied image quality metrics, the CNR-to-dose ratio confirms that EOSedge provides the best tradeoff between CNR and dose performances, compared to EOS-1st generation and to the DR system: for the lowest tested contrast insert with relative contrast 4.7 % (FIG. 11(d)), the CNRD values of EOSedge are 2.7 times to 4.6 times higher than those of EOS-1st generation, and 1.8 times to 3.4 times higher

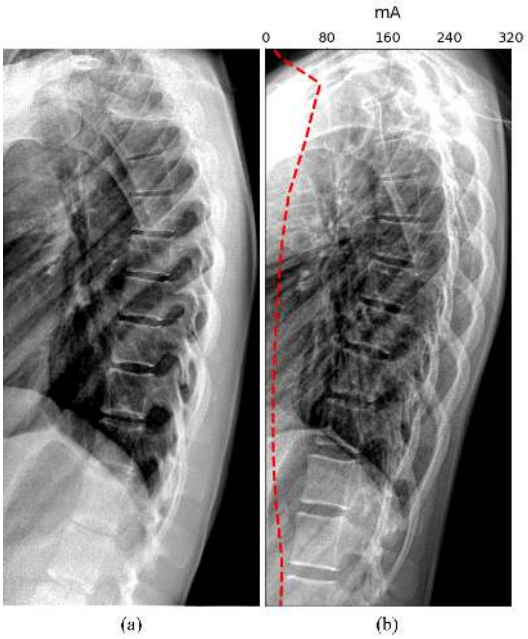

FIG. 16. (a) Localized lateral DR image of a thoracic spine. (b) Same area extracted from the corresponding lateral EOSedge low-dose (with Flex Dose) Full-Spine acquisition. The shape of the tube current modulation profile is shown as a dashed line.

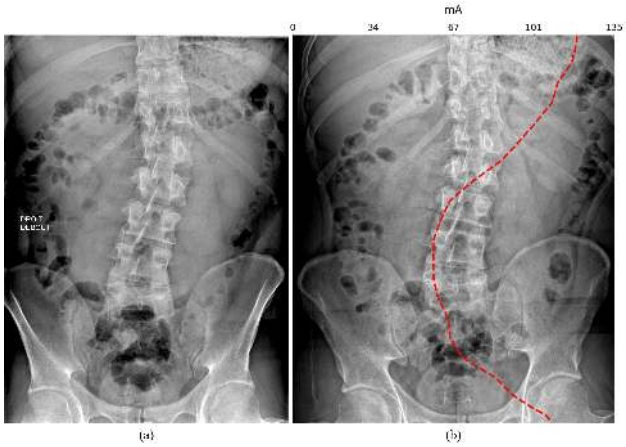

FIG. 17. (a) Localized frontal DR image of a lumbar spine. (b) Same area extracted from the corresponding frontal EOSedge low-dose (with Flex Dose) Full-Spine acquisition. The shape of the tube current modulation profile is shown as a dashed line.

FIG. 18. (a) Localized lateral DR image of a lumbar spine. (b) Same area extracted from the corresponding lateral EOSedge low-dose (with Flex Dose) Full-Spine acquisition. The shape of the tube current modulation profile is shown as a dashed line.

than those of the DR system. Of course, the stable behavior of EOSedge comes with an increased scan time for larger morphotypes (up to 8 times longer exposure time than for pediatric morphotypes).

The qualitative image quality assessment confirms the observed stability of EOSedge image quality, regardless of the local image attenuation. Observations on the RANDO phantom and on clinical data showed that the anatomical landmarks used in follow-ups of spinal deformities[9] with EOS-1st generation systems, can be detected with the same confidence level on EOSedge with Flex Dose. Detector dose ratios between EOSedge and DR were in the same order of magnitude in both the patient-based image quality and the phantom-based dosimetry studies (see Tables II, III and VIII). Variations may be due to the variability in terms of morphologies between the CIRS ATOM phantoms and the selected patients.

AEC is not the only design change between EOS-1st generation and EOSedge: the newly introduced X-ray photon-counting detector, as well as updated digital image processing chains (including image enhancement), significantly contribute to the final image quality of the displayed clinical images. Together with AEC, they provide significant dose reduction capabilities, with preserved anatomical landmark detection performances, whether compared against EOS-1st generation or DR.

Further additional studies could include a more detailed system characterization in terms of effective DQE[42], that seems to be a good candidate for the shortcomings of DQE mentioned in Section II D 1, and a clinical quantitative assessment of EOSedge image quality during routine care.

V. CONCLUSION

This study investigated organ and effective doses on pediatric and adult phantoms when imaging with two current standard imaging systems compared to the new EOSedge system. To our knowledge, EOSedge is the only slot-scanning system capable of full-body acquisition with a continuous AEC along the scan. Results showed that EOSedge provides significant dose reduction factors for full spine imaging in both adults and children compared to the other tested modalities, without compromising image quality.

We believe that this work could help raise awareness on the capabilities of modern X-ray systems, when equipped with appropriate AEC strategies, to perform ultra low-dose, high-quality, long-axis images.

ACKNOWLEDGEMENT

This work was sponsored by EOS Imaging, Paris, France. The second, third, fourth and fifth authors are full-time employees of EOS Imaging, Paris, France. The authors have no other conflict of interest to disclose. The authors are grateful to the Centre Médical Créqui (Lyon, France), where the DR room is located, and where the clinical data were collected.

[1] B. Ilharreborde, E. Ferrero, M. Alison, and K. Mazda, "EOS microdose protocol for the radiological follow-up of adolescent idiopathic scoliosis," European Spine Journal **25**, 526 (2016).

[2] A. N. Larson, B. A. Schueler, and J. Dubousset, "Radiation in spine deformity: state-of-the-art reviews," Spine deformity **7**, 386 (2019).

[3] K. R. Kutanzi, A. Lumen, I. Koturbash, and I. R. Miousse, "Pediatric exposures to ionizing radiation: carcinogenic considerations," International journal of environmental research and public health **13**, 1057 (2016).

[4] R. A. Kleinerman, "Cancer risks following diagnostic and therapeutic radiation exposure in children," Pediatric radiology **36**, 121 (2006).

[5] M. M. Doody, J. E. Lonstein, M. Stovall, D. G. Hacker, N. Luckyanov, C. E. Land, U. S. C. S. Collaborators, *et al.*, "Breast cancer mortality after diagnostic radiography: findings from the US Scoliosis Cohort Study," Spine **25**, 2052 (2000).

[6] P. J. Hashkes and R. M. Laxer, "103 - Management of juvenile idiopathic arthritis," in *Rheumatology (Sixth Edition)*, edited by M. C. Hochberg, A. J. Silman, J. S. Smolen, M. E. Weinblatt, and M. H. Weisman (Mosby, Philadelphia, 2015) pp. 851–861.

[7] R. Sauvagnac and M. Rigo, "Evolution of Early Onset Scoliosis under Treatment with a 3D-Brace Concept," Journal of Clinical Medicine **11**, 1186 (2022).

[8] S. Pasha, C. R. Rajapaske, R. Reddy, B. Diebo, P. Knott, B. C. Jones, D. Kumar, W. Zhu, E. Lou, N. Shapira, *et al.*, "Quantitative imaging of the spine in adolescent idiopathic scoliosis: shifting the paradigm from diagnostic to comprehensive prognostic evaluation," European Journal of Orthopaedic Surgery & Traumatology , 1 (2021).

[9] M. Yvert, A. Diallo, P. Bessou, J.-L. Rehel, E. Lhomme, and J.-F. Chateil, "Radiography of scoliosis: Comparative dose levels and image quality between a dynamic flat-panel detector and a slot-scanning device (EOS system)," Diagnostic and interventional imaging **96**, 1177 (2015).

[10] J. Dubousset, G. Charpak, I. Dorion, W. Skalli, F. Lavaste, J. Deguise, G. Kalifa, and S. Ferey, "A new 2D and 3D imaging approach to musculoskeletal physiology and pathology with low-dose radiation and the standing position: the EOS system," Bulletin de l'Academie nationale de medecine **189**, 287 (2005).

[11] S. Deschênes, G. Charron, G. Beaudoin, H. Labelle, J. Dubois, M.-C. Miron, and S. Parent, "Diagnostic imaging of spinal deformities: reducing patients radiation dose with a new slot-scanning X-ray imager," Spine **35**, 989 (2010).

[12] J. Damet, P. Fournier, P. Monnin, M. Sans-Merce, D. Ceroni, T. Zand, F. Verdun, and S. Baechler, "Occupational and patient exposure as well as image quality for full spine examinations with the EOS imaging system," Medical physics **41**, 063901 (2014).

[13] P. H. Pedersen, A. G. Petersen, S. E. Østgaard, T. Tvedebrink, and S. P. Eiskjær, "EOS micro-dose protocol: first full-spine radiation dose measurements in anthropomorphic phantoms and comparisons with EOS standard-dose and conventional digital radiology," Spine **43**, E1313 (2018).

[14] M. Halsey, L. A. Dolan, R. A. Hostin, R. D. Adobor, R. Dayer, E. Dema, and O. B. Letaif, "Scoliosis Research Society survey: brace management in adolescent idiopathic scoliosis," Spine Deformity **9**, 697 (2021).

[15] M. Söderberg and M. Gunnarsson, "Automatic exposure control in computed tomography–an evaluation of systems from different manufacturers," Acta radiologica **51**, 625 (2010).

[16] T. L. Herrmann, T. L. Fauber, J. Gill, C. Hoffman, D. K. Orth, P. A. Peterson, R. R. Prouty, A. P. Woodward, and T. G. Odle, "Best practices in digital radiography," Radiologic technology **84**, 83 (2012).

[17] M. K. Kalra, S. M. Rizzo, and R. A. Novelline, "Reducing radiation dose in emergency computed tomography with automatic exposure control techniques," Emergency radiology **11**, 267 (2005).

[18] T. H. Mulkens, P. Bellinck, M. Baeyaert, D. Ghysen, X. Van Dijck, E. Mussen, C. Venstermans, and J.-L. Termote, "Use of an automatic exposure control mechanism for dose optimization in multi–detector row CT examinations: clinical evaluation," Radiology **237**, 213 (2005).

[19] A. E. Papadakis, K. Perisinakis, and J. Damilakis, "Automatic exposure control in pediatric and adult multidetector CT examinations: a phantom study on dose reduction and image quality," Medical physics **35**, 4567 (2008).

[20] H. J. Brisse, L. Madec, G. Gaboriaud, T. Lemoine, A. Savignoni, S. Neuenschwander, B. Aubert, and J.-C. Rosenwald, "Automatic exposure control in multichannel CT with tube current modulation to achieve a constant level of image noise: experimental assessment on pediatric phantoms," Medical physics **34**, 3018 (2007).

[21] H. Kawata, S. Ookubo, and K. Hyoudou, "Influence of X-ray detector of automatic exposure control unit (AEC) on digital chest radiography," Nippon Hoshasen Gijutsu Gakkai Zasshi **57**, 1121 (2001).

[22] C. Moore, T. Wood, G. Avery, S. Balcam, L. Needler, A. Beavis, and J. Saunderson, "An investigation of automatic exposure control calibration for chest imaging with a computed radiography system," Physics in Medicine & Biology **59**, 2307 (2014).

[23] N. Marshall, "An examination of automatic exposure control regimes for two digital radiography systems," Physics in Medicine & Biology **54**, 4645 (2009).

[24] S. Alibek, M. Brand, C. Suess, W. Wuest, M. Uder, and H. Greess, "Dose reduction in pediatric computed tomography with automated exposure control," Academic radiology **18**, 690 (2011).

[25] P. Doyle, *Assessment and optimisation of digital radiography systems for clinical use*, Ph.D. thesis, University of Glasgow (2009).

[26] C. Martin, "Optimisation in general radiography," Biomedical imaging and intervention journal **3** (2007).

[27] E. Seeram, R. Davidson, S. Bushong, and H. Swan, "Radiation dose optimization research: Exposure technique approaches in CR imaging–A literature review," Radiography **19**, 331 (2013).

[28] J. T. Bushberg and J. M. Boone, *The essential physics of medical imaging* (Lippincott Williams & Wilkins, 2011).

[29] C. H. McCollough, M. R. Bruesewitz, and J. M. Kofler Jr, "CT dose reduction and dose management tools: overview of available options," Radiographics **26**, 503 (2006).

[30] J. Beucher, P. Désauté, K. Kyrgyzov, A. Lemoussu, P. Morichau-Beauchant, and H. Ouamara, "Radiological imaging method," WO Patent No. 2021094004A1 (2020).

[31] K. Goto, "Clinical Experience with Slot Radiography using SONIALVISION safire II, and Its Utility–Lower Limb Region–," Medical Now , 23 (2009).

[32] L. Bøtter-Jensen, S. W. McKeever, and A. G. Wintle, *Optically stimulated luminescence dosimetry* (Elsevier, 2003).

[33] M. Freitas, R. Alves, and E. Yoshimura, "Calibration of OSL dosimeters according to the IAEA code of practice for diagnostic radiology dosimetry TRS-457," Tech. Rep. (2010).

[34] I. Mrčela, T. Bokulić, J. Izewska, M. Budanec, A. Fröbe, and Z. Kusić, "Optically stimulated luminescence in vivo dosimetry for radiotherapy: physical characterization and clinical measurements in 60Co beams," Physics in Medicine & Biology **56**, 6065 (2011).

[35] S. B. Scarboro, D. Cody, P. Alvarez, D. Followill, L. Court, F. C. Stingo, D. Zhang, M. McNitt-Gray, and S. F. Kry, "Characterization of the nanoDot OSLD dosimeter in CT," Medical physics **42**, 1797 (2015).

[36] G. X. Ding and A. W. Malcolm, "An optically stimulated luminescence dosimeter for measuring patient exposure from imaging guidance procedures," Physics in Medicine & Biology **58**, 5885 (2013).

[37] M. W. Charles, "ICRP Publication 103: Recommendations of the ICRP," (2008).

[38] G. Poludniowski, G. Landry, F. Deblois, P. Evans, and F. Verhaegen, "SpekCalc: a program to calculate photon spectra from tungsten anode x-ray tubes," Physics in Medicine & Biology **54**, N433 (2009).

[39] J. H. Hubbell, "Tables of x-ray mass attenuation coefficients and mass energy-absorption coefficients," http://physics. nist.

gov/PhysRefData/XrayMassCoef/ (1996).
[40] Joint Committee for Guides in Metrology, "Evaluation of measurement data—guide to the expression of uncertainty in measurement," JCGM **100**, 1 (2008).
[41] J. Beutel, H. L. Kundel, Y. Kim, R. L. Van Metter, and S. C. Horii, *Handbook of medical imaging*, Vol. 3 (Spie Press, 2000).
[42] E. Samei, N. T. Ranger, A. MacKenzie, I. D. Honey, J. T. Dobbins III, and C. E. Ravin, "Effective DQE (eDQE) and speed of digital radiographic systems: an experimental methodology," Medical physics **36**, 3806 (2009).
[43] A. J. Abdi, B. R. Mussmann, A. Mackenzie, O. Gerke, B. Klaerke, and P. E. Andersen, "Quantitative Image Quality Metrics of the Low-Dose 2D/3D Slot Scanner Compared to Two Conventional Digital Radiography X-ray Imaging Systems," Diagnostics **11**, 1699 (2021).
[44] A. Clavel, P. Monnin, J. Létang, F. Verdun, and A. Darbon, "Characterising the EOS Slot-Scanning system with the effective detective quantum efficiency," Radiation protection dosimetry **169**, 319 (2016).
[45] E. B. Podgorsak, "Review of radiation oncology physics: a handbook for teachers and students," Vienna, Austria: IAE Agency , 13 (2003).
[46] W. A. Kalender, S. Buchenau, P. Deak, M. Kellermeier, O. Langner, M. van Straten, S. Vollmar, and S. Wilharm, "Technical approaches to the optimisation of CT," Physica Medica **24**, 71 (2008).
[47] S. Vollmar and W. Kalender, "Reduction of dose to the female breast as a result of spectral optimisation for high-contrast thoracic CT imaging: a phantom study," The British journal of radiology **82**, 920 (2009).
[48] G.-P. Chen, G. Noid, A. Tai, F. Liu, C. Lawton, B. Erickson, and X. A. Li, "Improving CT quality with optimized image parameters for radiation treatment planning and delivery guidance," Physics and Imaging in Radiation Oncology **4**, 6 (2017).
[49] C. Martin, P. Sharp, and D. Sutton, "Measurement of image quality in diagnostic radiology," Applied radiation and isotopes **50**, 21 (1999).
[50] A. Jones, C. Ansell, C. Jerrom, and I. Honey, "Optimization of image quality and patient dose in radiographs of paediatric extremities using direct digital radiography," The British journal of radiology **88**, 20140660 (2015).
[51] B. Escott, B. Ravi, A. Weathermon, J. Acharya, C. Gordon, P. Babyn, S. Kelley, and U. Narayanan, "EOS Low-Dose Radiography: A Reliable and Accurate Upright Assessment of Lower-Limb Lengths," The Journal of bone and joint surgery. American volume **95**, e1831 (2013).
[52] J. Greffier, A. Hamard, F. Pereira, C. Barrau, H. Pasquier, J. P. Beregi, and J. Frandon, "Image quality and dose reduction opportunity of deep learning image reconstruction algorithm for CT: a phantom study," European radiology **30**, 3951 (2020).
[53] A. Assi, Y. Chaibi, A. Presedo, J. Dubousset, I. Ghanem, and W. Skalli, "Three-dimensional reconstructions for asymptomatic and cerebral palsy children's lower limbs using a biplanar X-ray system: a feasibility study," European Journal of Radiology **82**, 2359 (2013).
[54] U. N. S. C. on the Effects of Atomic Radiation *et al.*, *Sources, Effects and Risks of Ionizing Radiation, United Nations Scientific Committee on the Effects of Atomic Radiation (UNSCEAR) 2016 Report: Report to the General Assembly, with Scientific Annexes* (United Nations, 2017).

Appendix A: OSL uncertainty calculation

The overall OSL measurement expanded uncertainty ($k = 2$)[40] was estimated at 11 %. This value combines the following uncertainties (as detailed in Table IX): readout uncertainty (6.4 %, deduced from the 5.5 % confidence interval given by the manufacturer); reference ionization air kerma calibration (0.8 %, as detailed on the calibration certificate), OSL calibration (4.0 %, deduced from data linear adjustment) and the beam quality variation in matter (8.0 %).

TABLE IX. OSL dose measurement uncertainties according to the GUM[40]; the symbol "⊓" stands for the assumption of a symmetric, rectangular a priori probability distribution, leading to an uncertainty value of $\sqrt{3} \cdot u(k = 1)$ (see Ref. 40, paragraph 4.4.5)

Type	Source	$U(k = 2)$	$u(k = 1)$	Type of Value	Uncertainty value
B	OSL readout	6.4 %	3.2 %	⊓	5.5 %
B	Reference ionization calibration	0.8 %	0.4 %	$U(k = 2)$	0.8 %
A	OSL air kerma calibration	4.0 %	2.0 %	$u(k = 1)$	2.0 %
B	$f_{Q,Q'} = 1$	8.0 %	4.0 %	⊓	6.9 %
	Combined uncertainty	11.0 %	5.5 %		

Appendix B: Child and Adult organ doses

Child and female adult organ dose values are available in Tables X and XI.

TABLE X. Child organ dose specified by ICRP 103[37] and effective dose calculation for DR, EOS-1st generation, EOSedge

Tissue	Weighting factors	Dose DR (mGy)	Dose EOS-1st generation[12] (mGy)	Dose EOSedge AP (mGy)
Brain	0.010	0.054	0.02	0.021
Thyroid	0.040	0.267	0.29	0.019
Lungs	0.120	0.137	0.22	0.023
Breast	0.120	0.189	0.28	0.033
Oesophagus	0.040	0.088	0.18	0.016
Liver	0.040	0.128	0.15	0.021
Bladder	0.040	0.108	0.15	0.027
Gonads	0.080	0.141	0.13	0.026
Stomach	0.120	0.175	0.25	0.032
Intestine	0.120	0.297	0.23	0.046
Red Bone Marrow	0.120	0.237	0.12	0.054
Remainder tissues	0.120	0.159	0.18	0.029
Effective dose (mSv)†		0.179	0.20	0.032

† Distributed organs, such as bone surface and skin, are missing from the effective dose calculated over non distributed organs; the sum of the weighting factors for the included organs is equal to 0.97

TABLE XI. Female adult organ dose specified by ICRP 103[37] and effective dose calculation for DR, EOS-1st generation, EOSedge AP and PA positioning

Tissue	Weighting factors	Dose DR (mGy)	Dose EOS-1st generation[12] (mGy)	Dose EOSedge AP (mGy)	Dose EOSedge PA (mGy)
Brain	0.01	0.134	0.38	0.053	0.052
Thyroid	0.04	0.512	0.45	0.076	0.050
Lung	0.12	0.421	0.27	0.055	0.053
Breast	0.12	0.385	0.34	0.077	0.075
Oesophagus	0.04	0.308	0.45	0.050	0.049
Liver	0.04	0.566	0.24	0.072	0.066
Intestine	0.12	1.001	0.28	0.122	0.113
Bladder	0.04	0.510	0.2	0.182	0.166
Ovaries	0.08	0.294	0.12	0.159	0.177
Stomach	0.12	0.947	0.42	0.090	0.047
Red Bone Marrow	0.12	0.358	0.2	0.090	0.087
Remainder tissues	0.12	0.817	0.28	0.098	0.089
Effective dose (mSv)†		0.572	0.29	0.092	0.084

† Distributed organs, such as bone surface and skin, are missing from the effective dose calculated over non distributed organs; the sum of the weighting factors for the included organs is equal to 0.97